AIAA JOURNAL
Vol. 48, No. 2, February 2010

Intermittent Bursting of a Laminar Separation Bubble on an Airfoil

Jaber H. Almutairi,* Lloyd E. Jones,† and Neil D. Sandham‡
University of Southampton, Southampton, England SO17 1BJ, UnitedKingdom

DOI: 10.2514/1.44298

Large eddy simulation of flow around a NACA-0012 airfoil at a Reynolds number of 50,000 has been used to study the behavior of a laminar separation bubble near stall. The effects of the subgrid-scale model and explicit filtering were studied for a test case in which direct numerical simulation results were available. It was found that a method incorporating a mixed-time-scale model in addition to explicit filtering gave improved results compared with a method with filtering alone. Statistical results as well as snapshots of the flow below stall exhibit good agreement with the direct numerical simulations. For a configuration near stall, the effect of the spanwise domain width was investigated by increasing the spanwise length from 20 to 50% chord. Two-point velocity correlations showed a significant improvement for the wider computational domain, in which the simulation was able to capture a low-frequency flow oscillation, in which intermittent bursting of the bubble was observed. The bubble bursting observed here is more irregular than in experiments at higher Reynolds number. The amplitude and frequency are compared with experimental results and with an unsteady viscous-inviscid interaction method which is shown to be capable of capturing unsteady behavior during stall.

Nomenclature

a, b	=	filtering coefficients
C_d, C_t	=	mixed time scale model parameters
C_f	=	skin-friction coefficient
C_L	=	lift coefficient
C_p	=	pressure coefficient
c	=	chord
$\bar{F}$	=	filtered inviscid fluxes vector
f	=	frequency of the flow oscillation
$\bar{G}$	=	filtered viscous fluxes vector
H	=	shape factor $H = \delta^*/\theta$
L_z	=	domain length in spanwise direction
M	=	reference Mach number
Pr	=	Prandtl number
$\bar{p}$	=	filtered pressure
Q	=	conservative flow variables vector or second invariant of the velocity gradient tensor
$\bar{Q}$	=	filtered conservative flow variables vector
q	=	flow variable
$\bar{q}$	=	filtered flow variable
$\tilde{q}$	=	Favre filtered flow variable
q_{SGS}	=	velocity scale for unresolved flow
q'	=	small scale of the flow variable
Re	=	Reynolds number based on the freestream conditions and chord length
St	=	Strouhal number $St = fc \sin\alpha/U$
$\bar{S}_{ij}$	=	strain rate tensor
$\tilde{T}$	=	filtered temperature
U	=	freestream velocity
u_τ	=	friction velocity
υ_t	=	eddy viscosity
α	=	angle of attack incidence
γ	=	ratio of specific heats
$\bar{\Delta}$	=	filter size
δ_{ij}	=	Kronecker delta
δ^*	=	displacement thickness
θ	=	momentum thickness
μ	=	dynamic viscosity
ν	=	fluid kinematic viscosity
$\bar{\rho}$	=	filtered fluid density
τ_{ij}	=	subgrid scale stress tensor
τ_{kk}	=	isotropic part of the subgrid scale Reynolds stress tensor
τ_w	=	shear wall stress
$\langle\,\rangle$	=	averaging over z

Received 11 March 2009; revision received 16 June 2009; accepted for publication 20 Sept. 2009.

*Ph.D. Student, School of Engineering Sciences.
†Research Fellow, School of Engineering Sciences.
‡Professor of Aerospace Engineering, School of Engineering Sciences; n.sandham@soton.ac.uk. Senior Member AIAA.

I. Introduction

STALL is a critical phenomenon that limits the performance of lifting surfaces. Stall behavior at low Reynolds numbers is currently of much interest due to applications to micro air vehicles and unmanned air vehicles where there may be laminar separation near the leading edge. Airfoil stall can be classified into three main types: leading-edge stall, thin-airfoil stall and trailing-edge stall [1]. The leading-edge stall phenomenon occurs when the flow separates near the leading edge without any reattachment downstream of the separation. In thin-airfoil stall the flow reattaches and becomes turbulent, with the point of reattachment shifting downstream as the angle of attack is increased. In trailing-edge stall, the separation of the turbulent boundary layer first occurs at a point near the trailing edge and then moves toward the leading edge as the angle of attack is increased.

Early studies, such as Gaster [2] and Horton [3], made important contributions to understanding the behavior of laminar separation bubbles, which play a role in the first two of these types of stall. Horton [3] used the experimental results from Gaster [2] to develop a semi-empirical method for predicting the growth and bursting of laminar separation bubbles. Horton found that the bursting occurred when the turbulent boundary layer fails to reattach and when the theoretical pressure recovery does not intersect the inviscid pressure distribution.

Laminar separation bubbles are classically described as being either short or long (see, e.g., Gaster [2]). As the incidence is increased a short bubble may burst, i.e., fail to reattach. This can lead to fully stalled flow, or else the separated shear layer may reattach and form a long bubble. Prediction of laminar separation bubbles was successfully achieved by Drela and Giles [4] who used a steady viscous-inviscid interaction method. They used the Euler equations to describe the inviscid flow and two equations of the integral

boundary layer, which are coupled by the displacement thickness to describe the viscous flow.

Unsteady separation bubbles exhibiting bubble bursting and low-frequency oscillation during stall have been observed experimentally. For example, Zaman et al. [5] made some remarkable observations of a low-frequency phenomenon during an experimental and numerical study of flow around 2-D airfoils at low Reynolds numbers in the range of 0.15×10^5–3×10^5. They concluded that the flow oscillations were different from other fluid mechanical phenomena such as bluff-body shedding, flow over cavities, and supersonic jet screech. They also specified the types of airfoils where the low-frequency oscillations can occur, which are airfoils that exhibit either trailing-edge stall or thin-airfoil stall. The fluctuations of the lift coefficient were found to be as much as 50% of the mean lift coefficient. In a later study, Bragg et al. [6] tested an LRN-1007 airfoil at Reynolds numbers between 3×10^5 and 1.25×10^6 at angles-of-attack α between 14.4 deg and 16.6 deg. The lift coefficient exhibited a low-frequency oscillation, and they found that as α was increased, the Strouhal number (defined as $St = fc \sin\alpha / U$ where f is the frequency of the flow oscillation, c is the chord length, α is the angle of attack, and U is the freestream velocity) tended to increase. Strouhal numbers associated with the oscillation lay in the range of 0.017 to 0.03, which is around 10 times lower than the Strouhal number for bluff-body shedding. Broeren and Bragg [7] performed another experiment, using the same airfoil geometry at $Re = 3 \times 10^5$ and $\alpha = 15$ deg, in which the phase average on the upper surface of the airfoil clearly showed a growth of the leading-edge separation bubble and trailing-edge separation until they merged, causing full boundary-layer separation and stall. Rinoie and Takemura [8] performed a similar experimental study of a NACA-0012 airfoil at a Reynolds number of 1.3×10^5 and $\alpha = 10$ deg and 11.5 deg that provided insight into the mechanism behind the low-frequency oscillation. At $\alpha = 10$ deg, they detected a steady, short laminar separation bubble near the leading-edge with a length of approximately 10% chord. They also observed the formation of a long bubble with a length of 35% chord at $\alpha = 11.5$ deg by averaging the velocities. At this angle of attack the flow exhibited a regular low-frequency oscillation in which it switched between a short laminar separation bubble of about 10% chord near the leading edge and a fully separated flow. Phase-averaged measurements indicated that the flow oscillations formed a short laminar separation bubble, similar to that at $\alpha = 10$ deg, at a phase angle $\phi = 0$ deg, and then the flow separated to form a long bubble between $\phi =$ 45 deg and $\phi = 90$ deg with 30% and 50% chord, respectively. The flow separated completely without any reattachment between $\phi =$ 90 deg and $\phi = 270$ deg, and a short laminar separation bubble was formed again at $\phi = 315$ deg. To date, this phenomenon has not been studied by direct or large-eddy simulation. Sandham [9] showed that an unsteady viscous-inviscid interaction method reproduces some of the characteristics of the low-frequency oscillation but that such models need further development and calibration, for example, against numerical simulations, which are becoming increasingly feasible.

The increasing capacity and performance of computers allow the study of laminar separation bubble by high accuracy numerical methods, such as direct numerical simulation (DNS) and large-eddy simulation (LES). The first 2-D simulations were presented for flow by Pauley et al. [10]. Three-dimensional direct numerical simulation was presented by Alam and Sandham [11] and Spalart and Strelets [12] on flow over a flat plate to study the behavior of laminar separation bubbles. The simulation of Spalart and Strelets [12] showed the complete process of transition to turbulence for a flow in which they observed that wavering of the shear layer occurred within the transition region, followed by Kelvin–Helmholtz vortices that were amplified to produce a 3-D flow without pairing. A large-eddy simulation of a flat plate with a semicircular leading edge by Yang and Voke [13] showed that the free shear layer of the laminar separation bubble becomes inviscidly unstable by means of the Kelvin–Helmholtz instability mechanism. Two-dimensional instability waves grow downstream until they are converted by secondary instability into 3-D motions. Streamwise vortices are formed in the vicinity of the reattachment point, which rolled up further downstream of the laminar separation bubbles, leading to a breakdown to turbulence.

One of the first attempts to simulate a 3-D flow over a nonsymmetrical lifting body configuration, such as the airfoil by DNS, was performed by Hoarau et al. [14]. They used the DNS to simulate an incompressible flow around a NACA-0012 with a very low Reynolds number (800) and at $\alpha = 20$ deg. They found that the vortices were shed from the upper surface of the airfoil as a result of the propagation of von Kármán instability instead of the Kelvin–Helmholtz instability because of the very low Reynolds number. The quasi-3-D LES (only 4 points across span) of Yuan et al. [15] on an SD7003 airfoil at a Reynolds number of 60,000 was able to capture the most important physical behavior in the laminar-turbulent transitional flows, but the results may be affected by freestream turbulence and the effect of the inadequate spanwise width of the computational domain.

Jones et al. [16] presented the first resolved DNS of flow around an NACA-0012 airfoil at Reynolds number of 50,000 and $\alpha = 5$ deg. They triggered the transition to turbulence by adding volume forcing to the momentum equations and found that the turbulence self-sustains due to the absolute instability of the vortex shedding. They observed that the behavior of the laminar separation bubble in the forced case was different than the unforced case and that forcing is able to improve the aerodynamic performance of the airfoil.

Recently the laminar-turbulence transition process was also studied experimentally by Zhang et al. [17], who applied a quasi-3-D particle image velocimetry (PIV) technique on the SD7003 airfoil at a Reynolds number of 20,000 and 60,000 and incidence of 4 deg, to study the vortex shedding in the transition of the LSB and the propagation of the vortices on the turbulent boundary layer. They verified the DNS results of Spalart and Strelets [12] and the LES results of Yang and Voke [13] regarding the primary role of the Kelvin–Helmholtz mechanism on the vortex shedding of the vortices and the subsequent breakdown to turbulence phenomenon, and thus, the ability of the numerical methods to describe the laminar-turbulence transition and the flow physics of low Reynolds number airfoils. Windte et al. [18] have shown that 2-D unsteady RANS simulations can provide comparable results with the experiments in terms of the transition position and the size of the laminar separation bubble.

It is clear that LES is a promising technique for low Reynolds number aerodynamics where the flows are often dominated by laminar separation and transition to turbulence. In the current study, LES has been applied to low Reynolds number flow around a NACA-0012 airfoil to study the behavior of a laminar separation bubble (LSB) near stall. The simulations use larger spanwise length than previous LES at lower incidence. The aim is to extend LES into the stall region to understand better the bursting of separation bubbles. Comparisons are made with experiments and with results from an unsteady viscous-inviscid interaction model.

II. Governing Equations

A. Filtered Navier–Stokes Equations

Any flow variable q can be decomposed into two parts $q = \bar{q} + q'$, where $\bar{q}$ is the large-scale part, which can be resolved by LES, and q' is the small scale part of the flow, which must be modeled by a subgrid-scale (SGS) model. It is convenient to define $\bar{q}$ as the flow variable filtered by a low-pass filter. For compressible flows it is additionally useful to use $\tilde{q} = \overline{\rho q}/\bar{\rho}$ as a Favre filtered flow variable. The conservative and dimensionless form of the 3-D, unsteady, filtered Navier–Stokes (N-S) equations for a viscous compressible flow can be written as

$$\frac{\partial \bar{Q}}{\partial t} + \frac{\partial \bar{F}_j}{\partial x_j} = \frac{\partial \bar{G}_j}{\partial x_j} \tag{1}$$

where $\bar{Q}$ is a vector containing the filtered conservative flow variables, $\bar{F}$ is the filtered inviscid flux vector, and $\bar{G}$ is the filtered viscous flux vector. The variable and flux vectors can be written in

dimensionless form (using freestream velocity, temperature, and density as reference quantities and the airfoil chord as the reference length scale) as

$$\bar{Q} = \begin{bmatrix} \bar{\rho} \\ \bar{\rho}\tilde{u}_1 \\ \bar{\rho}\tilde{u}_2 \\ \bar{\rho}\tilde{u}_3 \\ \bar{\rho}\left(\frac{\tilde{T}}{\gamma(\gamma-1)M^2} + \frac{\tilde{u}_1\tilde{u}_1+\tilde{u}_2\tilde{u}_2+\tilde{u}_3\tilde{u}_3}{2}\right) \end{bmatrix}, \qquad \bar{F}_j = \tilde{u}_j\bar{Q} + \begin{bmatrix} 0 \\ \delta_{1j}\bar{p} \\ \delta_{2j}\bar{p} \\ \delta_{3j}\bar{p} \\ \bar{p}\tilde{u}_j \end{bmatrix}$$

$$\bar{G}_j = \begin{bmatrix} 0 \\ \bar{\sigma}_{1j} - \tau_{1j} \\ \bar{\sigma}_{2j} - \tau_{2j} \\ \bar{\sigma}_{3j} - \tau_{3j} \\ \bar{\sigma}_{kj}\tilde{u}_k + \bar{q}_j \end{bmatrix} \tag{2}$$

where $\bar{\rho}$ refers to the filtered fluid density, $(\tilde{u}_1, \tilde{u}_2, \tilde{u}_3) = (\tilde{u}, \tilde{v}, \tilde{w})$ refers to the filtered velocity vector in Cartesian coordinates, $\tilde{T}$ refers to the filtered temperature, γ refers to the ratio of specific heats, and M refers to the reference Mach number. The heat flux $\bar{q}_j$ is defined as

$$\bar{q}_j = \frac{\mu(\tilde{T})}{(\gamma-1)RePrM^2}\frac{\partial\tilde{T}}{\partial x_j} \tag{3}$$

where the dynamic viscosity for air can be calculated from Sutherland's law as

$$\mu(\tilde{T}) = \tilde{T}^{\frac{3}{2}}\frac{1+C}{\tilde{T}+C}, \quad (\text{where } C = 0.3686) \tag{4}$$

where the filtered temperature $\tilde{T}$ is related to both the filtered density $\bar{\rho}$ and the filtered pressure $\bar{p}$ by the ideal gas law

$$\tilde{T} = \gamma M^2\frac{\bar{p}}{\bar{\rho}} \tag{5}$$

The viscous stress tensor $\bar{\sigma}_{ij}$ can be written as

$$\bar{\sigma}_{ij} = \frac{\mu(\tilde{T})}{Re}\left(\frac{\partial\tilde{u}_i}{\partial x_j} + \frac{\partial\tilde{u}_j}{\partial x_i} - \frac{2}{3}\delta_{ij}\frac{\partial\tilde{u}_k}{\partial x_k}\right) \tag{6}$$

where δ_{ij} is the Kronecker delta, and Re is the Reynolds number based on the freestream conditions and chord- length. The quantity τ_{ij} is the SGS stress tensor that expresses the effect of the small scales on the residual stress:

$$\tau_{ij} = \overline{\rho u_i u_j} - \overline{\rho u_i}\,\overline{\rho u_j}/\bar{\rho} \tag{7}$$

This term is modeled based on the concept of the eddy viscosity, and so the stress tensor can be written as

$$\tau_{ij} - \frac{1}{3}\delta_{ij}\tau_{kk} = 2\upsilon_t\bar{S}_{ij} \tag{8}$$

where τ_{kk} is the trace of the SGS Reynolds stress tensor and υ_t refers to the eddy viscosity, which is obtained from an SGS model. The strain rate tensor is given as

$$\bar{S}_{ij} = \frac{1}{2}\left(\frac{\partial\tilde{u}_i}{\partial x_j} + \frac{\partial\tilde{u}_j}{\partial x_i}\right) \tag{9}$$

B. Mixed-Time-Scale Model

The mixed-time-scale (MTS) model, developed by Inagaki et al. [19], has been used as the SGS model in the present study. The model is advantageous in the present application because it is local, turns off in laminar flow, and does not require an additional wall-damping function. In the MTS model, the eddy viscosity is expressed as

$$\upsilon_t = C_d T_s q_{\text{SGS}}^2 \tag{10}$$

where q_{SGS} is the velocity scale, which can be calculated by explicitly filtering the velocity field using

$$q_{\text{SGS}}^2 = (\bar{u} - \tilde{\bar{u}})^2 \tag{11}$$

where $\tilde{()}$ denotes a filtering operation, using a simple top-hat filter. When this expression for the velocity scale q_{SGS} is employed, the eddy viscosity υ_t in the laminar flow region will be guaranteed to approach zero, as long as the flow is fully resolved and the velocity scale (q_{SGS}) approaches zero. C_d is a fixed model parameter, and the time scale T_s is obtained from the following equation:

$$T_s^{-1} = \left(\frac{\bar{\Delta}}{q_{\text{SGS}}}\right)^{-1} + \left(\frac{C_t}{|\bar{S}|}\right)^{-1} \tag{12}$$

The two model parameters C_d and C_t are set to be 0.03 and 10, respectively. These values were set from initial tests for turbulent channel flow with our code and have since been left unchanged [20].

III. Numerical Procedure

The numerical method is essentially the same as that used by Jones et al. [16], originally written and validated by Sandham et al. [21], to solve the Navier–Stokes equations for a compressible flow. The code employs a fourth order accurate central difference scheme for spatial discretization of the interior points, whereas a Carpenter fourth order accurate scheme [22] is used to treat the points on the boundary. Temporal discretization is performed using a fourth order explicit Runge–Kutta scheme.

Unwanted high frequency oscillations can be alleviated by the use of filtering. Spatial filtering is carried out by applying explicit or implicit low-pass filters to the unfiltered DNS according to the following equation:

$$\hat{q}_i + a_1(\hat{q}_{i-2} + \hat{q}_{i+2}) + a_2(\hat{q}_{i-1} + \hat{q}_{i+1}) = b_1 q_i + \frac{b_2}{2}(q_{i-1} + q_{i+1}) + \frac{b_3}{2}(q_{i-2} + q_{i+2}) + \frac{b_4}{2}(q_{i-3} + q_{i+3}) \tag{13}$$

where $\hat{q}_i$ represents the filtered value at point i, whereas the original (unfiltered) value is q_i at the same point i. This equation has been studied in detail in Lele [23]. Most of the necessary coefficients in Eq. (13) are derived by matching the coefficients of Taylor series based on the degree of accuracy order required for such a numerical scheme. Visbal and Rizzetta [24] studied low-pass spatial filtering and demonstrated its superior performance for compressible LES on a stretched, curvilinear grid when it is incorporated into high-order finite difference schemes. They found that to maintain numerical stability for a relatively coarse grid, and thus suppress the numerical oscillations that arise from the unresolved scales obtained by compact-differencing schemes, it is necessary to add a compact filter scheme with equal or higher order of accuracy than the spatial discretization. For example, the fourth order compact scheme should be combined with a filter of at least fourth order accuracy. In the present work, the fourth order tridiagonal scheme has been used and constructed from Eq. (13) by setting $a_1 = 0$, $a_2 = 0.49$, $b_1 = 0.9925$, $b_2 = 0.9900$, $b_3 = -0.0025$, and $b_4 = 0$.

Spectral analysis of the filter uses the transfer function of Eq. (13) [23]

$$\text{TF}(kh) = \frac{b_1 + b_2\cos(kh) + b_3\cos(2kh) + b_4\cos(3kh)}{1 + 2a_1\cos(2kh) + 2a_2\cos(kh)} \tag{14}$$

where k is the wavenumber and h is the spacing between grid points. Setting the free parameter a_2 close to 0.5 produces a spectral response with almost sharp cut-off characteristics. Figure 1 shows the effect of increasing a_2 toward 0.5 on the filtering transfer function.

In many practical applications, it is not necessary to apply the low-pass filter in full every time step but partially according to the following equation

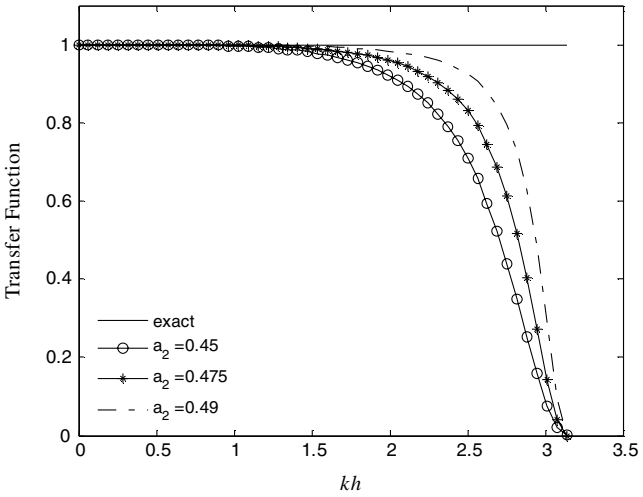

Fig. 1 The filter transfer function for different values of a_2.

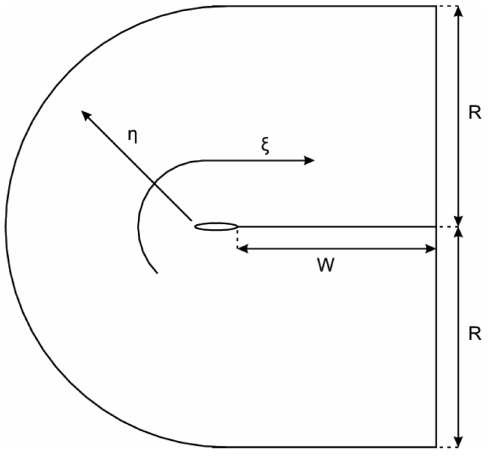

Fig. 2 Domain boundaries and coordinate system around NACA-0012 airfoil [26].

$$\bar{Q} = Q - \sigma(Q - \hat{Q}) \tag{15}$$

where $\bar{Q}$ represents the resulting filtered function, Q is the unfiltered function, $\hat{Q}$ is the filtered function, and σ is a constant between 0 and 1. If σ is 0 that means there is no filtering and if it is 1 then the whole function is filtered ($\bar{Q} = \hat{Q}$). Bogey and Bailly [25] suggested setting σ between 0.1 and 0.2 to get a stable numerical solution. In this work, the LES is performed by explicitly filtering the conservative variables.

IV. Validation Against Direct Numerical Simulation Results ($Re = 50,000$ and $\alpha = 5$ deg)

The numerical code has been validated by performing simulations with Mach number $M_\infty = 0.4$ at an incidence of 5 deg and a Reynolds number of 50,000. A grid of 637×375 was generated and data were compared with the DNS of Jones [26] which used a grid of 2570×692. The 2-D simulation was then extended to a 3-D simulation with 32 grid points in the spanwise direction and compared with DNS results on a $2570 \times 692 \times 96$ grid. The computational cost of the LES was a factor of 22 less than the computational cost of the DNS.

The 3-D validation computations were conducted in two ways: first, by applying the LES without using any SGS model, i.e., relying on filtering alone, and second, by adding the MTS model. In these tests a time-dependent forcing was added to trigger transition to turbulence. The low-amplitude forcing was applied inside the separated shear layer and was removed after it triggers the transition to turbulence because this process self-sustains [16].

The C-mesh, geometry parameters and the coordinate system are depicted in Fig. 2. The main grid parameters of both 2- and 3-D simulations are summarized in Table 1. The columns W, R, and Total length correspond to the wake length, radius, and total domain length, respectively, in airfoil chords, whereas N_ξ and N_η represent the numbers of grid points in the curvilinear directions ξ and η, respectively. The columns PS, SS, NW, and Total points correspond to the numbers of cells on the pressure side, on the suction side, in the wake, and total cells, respectively. Grids were refined by an iterative process. For the chosen filter coefficient the simulation was run for a short time and under-resolved regions (revealed by grid-to-grid point oscillations) were identified. The grid was refined in these regions and the run continued. The process was repeated until a good grid was found. For the initial validations we consider 2-D filtered Navier–Stokes simulations and 3-D LES compared with reference DNS in 2-D and 3-D, respectively. An integral characteristic boundary condition [27] is applied at the freestream boundary (η^+), while a zonal characteristic boundary condition [28] is applied at the downstream exit boundary ($\xi^\pm$). An adiabatic, no-slip condition is applied at the airfoil surface and a spanwise periodic boundary condition is applied to the simulation every substep of the Runge–Kutta time stepping. Statistics are obtained by averaging in time and for the 3-D calculation also in the homogeneous spanwise direction.

A. Two-Dimensional Results

The numerical results from the filtered Navier–Stokes simulation were obtained without a subgrid-scale model but with filtering every time step. To obtain a result that was as accurate as possible, a parametric study was performed (not shown here) using different values of the filtering coefficient (σ) to find the optimum value which gives the best solution comparing with the DNS for a fixed grid; $\sigma = 0.14$ was found to be the optimum value. The simulation was performed with a time step of 1.55×10^{-4}. Statistical data describing the aerodynamics of the simulation, such as pressure coefficient and skin-friction, were computed after the flow had passed an initial transient stage. Time averaging for the simulation was taken over 60,000 time steps, which corresponded to 9.3 nondimensional time units. The lift coefficient (C_L) oscillates periodically around a mean of 0.495, which agrees with the DNS results [26] as demonstrated in Fig. 3. The frequency of the filtered N-S simulation is $f = 3.27$ which is very close to the DNS ($f = 3.32$). Compared with the DNS, C_L from the 2-D filtered Navier–Stokes simulation is slightly more regular, presumably due to the decrease in degrees of freedom associated with the coarser mesh. From a Fourier analysis, the DNS signal has an additional lower frequency mode ($f = 1.98$) present with a fifth of the amplitude of the dominant shedding mode.

The pressure coefficient from the 2-D filtered Navier–Stokes simulation is compared with DNS in Fig. 4, where it can be seen that the 2-D filtered Navier–Stokes simulation matches the DNS very well. This figure shows the strong adverse pressure gradient near the leading edge that causes the separation to occur, followed by a

Table 1 Comparison of grid parameters for validation study ($Re = 50,000$ and $\alpha = 5$ deg)

Simulation	W	R	Total length	N_ξ	N_η	N_z	L_z/c	Ps	SS	NW	Total points
2-D filtered N-S	5	7.3	14.2	637	375	-	-	78	190	185	238,875
LES, 3-D	5	7.3	14.2	637	375	32	0.2	78	190	185	7,644,000
DNS, 3-D	5	7.3	14.2	2570	692	96	0.2	292	792	753	170,730,240

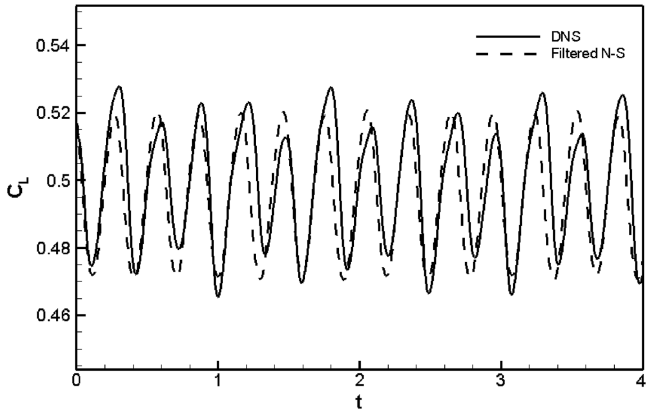

Fig. 3 Comparison of time-dependent lift coefficient for 2-D simulations ($\alpha = 5$ deg).

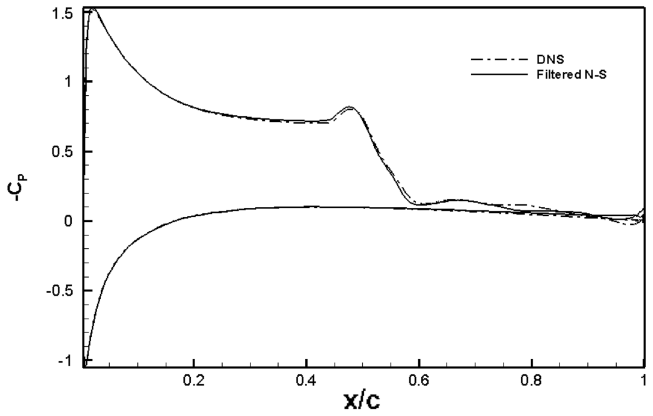

Fig. 4 Comparison of 2-D pressure coefficient between DNS and 2-D filtered Navier–Stokes simulation ($\alpha = 5$ deg).

pressure plateau that indicates the length of the dead-air region in the laminar separation bubble. Inspection of Fig. 4 confirms the observation of Ripley and Pauley [29] concerning the existence of a spike at the end of the pressure plateau for 2-D simulations. The rapid increase in the pressure that occurs after the pressure plateau is a result of the roll up of vortices at the back of the bubble before vortex shedding.

The unsteadiness of the simulation can be observed by taking snapshots of vorticity. For the purpose of validation, contours of instantaneous vorticity obtained from the 2-D filtered Navier–Stokes simulation are depicted in Fig. 5a, in which it can be observed that a separated shear layer forms on the suction side of the airfoil after flow separation near the leading edge and then becomes unstable at the middle of the airfoil chord, where large-scale vortices are generated and convect downstream, leading to the development of vortex shedding. The successful calculation of this flow behavior can be confirmed when comparing Fig. 5a with the DNS vorticity in Fig. 5b taken from Jones [26]. From these figures, it is obvious that the vorticity obtained by 2-D filtered Navier–Stokes simulation is very close to the DNS, without significant numerical oscillations.

B. Three-Dimensional Results

The 2-D solution is taken as an initial condition for the 3-D simulations, which are required for a realistic representation of the flow. Forcing is applied at the early stages of the 3-D simulation to trigger transition to turbulence (see [26] section 2.2.10 for forcing details). Then the forcing is removed and the simulation is run further. The statistical data are dumped and the flowfield is stored every 10,000 time steps, with a time step of 1.55×10^{-4}. Adequate mesh resolution is important to obtain an accurate solution and to ensure that the large eddies in the flow are resolved. Wall units y^+, Δx^+, and Δz^+, are normally used to check the mesh resolution for a particular grid. The friction velocity u_τ is used to calculate $y^+ = y u_\tau / \nu$, where $u_\tau = \sqrt{|\tau_w|/\rho}$ is obtained using the absolute value of the wall shear stress τ_w, and Δx^+ and Δz^+ are calculated as $\Delta x^+ = \Delta x u_\tau / \nu$ and $\Delta z^+ = \Delta z u_\tau / \nu$, respectively. The LES usually needs streamwise and spanwise mesh resolutions of approximately $\Delta x^+ \leq 50$ and $\Delta z^+ \leq 20$, respectively. Figure 6 shows the variation of the streamwise and the spanwise resolutions on the suction side of the airfoil, showing that in both cases the mesh resolutions over the transitional and turbulent regions satisfy the LES resolution requirements (we have $\Delta x^+ < 15$ and $\Delta z^+ < 21$). Table 2 shows a comparison of mesh resolutions between the DNS and LES for the simulation with $\alpha = 5$ deg at $Re = 50,000$. The first grid point from the surface in the LES has $y_1^+ = 0.849$, which is the worst value in the turbulent region (at $x/c = 0.7$), and with five grid points in $y^+ < 10$. The existence of relatively large oscillations near the geometric singularity of the trailing edge limits the coarseness of grid, because any further decrease of resolution may cause these oscillations to grow severely.

Comparisons between the LES and DNS have been made based on the momentum and displacement thickness in Fig. 7, in which it can be clearly seen that the LES solution matches the DNS very well. Figure 8 shows the LES solution for isosurfaces of the second invariant of the velocity gradient tensor:

$$Q = -\frac{1}{2}\frac{\partial u_i}{\partial x_j}\frac{\partial u_j}{\partial x_i} = -\frac{1}{2}(S_{ij}S_{ij} - \Omega_{ij}\Omega_{ij}) \tag{16}$$

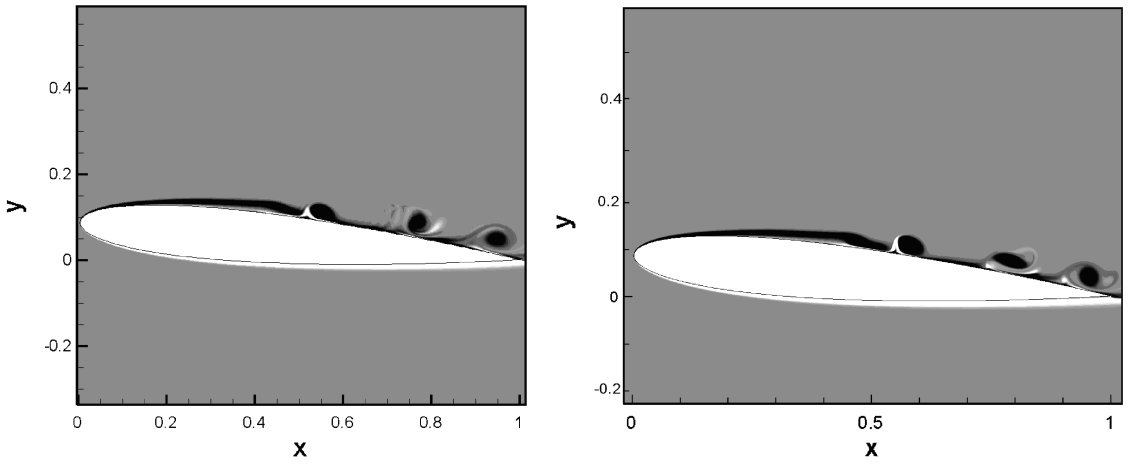

a) b)

Fig. 5 Vorticity contour for 2-D simulation at $Re = 50,000$ with $\alpha = 5$ deg using 10 levels ±50 obtained from a) 2-D filtered Navier–Stokes simulation and b) DNS (taken from Jones [26]).

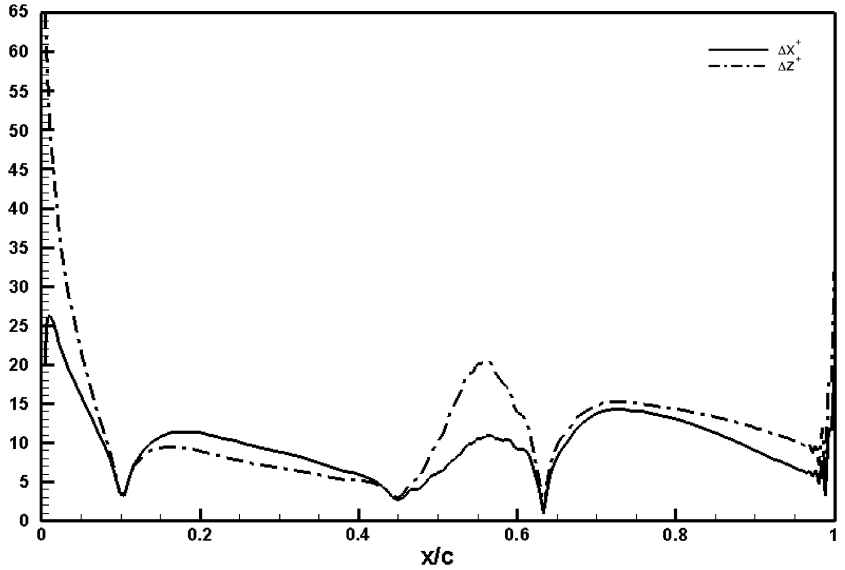

Fig. 6 Streamwise and spanwise mesh resolution on the suction side in the wall unit obtained from 3-D LES ($\alpha = 5$ deg, without SGS).

over the upper surface of the airfoil. Positive values of the Q-criterion locate regions where rotation dominates over strain rate. From this figure, it is clear that the process of breakdown to turbulence is captured in the LES, in qualitative agreement with the DNS of Jones et al. [16]. Starting from the leading edge, the shear layer is detached from the wall with a laminar 2-D behavior. The transition becomes visible in which a small distortion of the shear layer takes place and the three-dimensionality of the flow starts to grow. Large-scale structures form and then break down into small structures followed by fully 3-D turbulent flow.

C. Further Comparisons Including Effect of Subgrid Scale Model

To assess the effect of the SGS model on the LES solution, the MTS model was included, and a new simulation was run for the same grid using the same procedure as for the case without an SGS model. Results obtained from this simulation demonstrate the benefits of using the SGS model. For example, the pressure distributions over the airfoil obtained by both LES simulations clearly match the DNS without any significant error, as illustrated in Fig. 9. However, the skin-friction profile, which is depicted in Fig. 10, is more sensitive. It is clear that the LES with the SGS model is closer to the DNS than the LES without SGS, specifically under the recirculation vortex at the back of the bubble and in the region near reattachment, however, both LES cases underpredict skin friction compared with the DNS after reattachment. The solution on the pressure side is improved with the SGS model, even though that boundary layer is laminar. This is presumably an indirect effect due to the improved modelling of the bubble, which is transmitted to the pressure side by the change in the potential flow. It is concluded that the incorporation of the SGS model is beneficial in the present configuration, and this formulation is applied for the remaining LES in this paper.

V. Effect of the Computational Domain Width on an Airfoil Near Stall

The objective of this section is to provide insight into the behavior of the laminar separation bubble at the onset of stalling for an NACA-0012 airfoil at $M_\infty = 0.4$, and $Re = 50,000$. To accomplish this,

Table 2 Comparison of grid resolution in wall units between DNS and LES results at maximum C_f

Simulation	Δx^+	Δz^+	No. of points for $y^+ < 10$
LES, 3-D	4.34	5.39	5
DNS, 3-D	3.36	6.49	9

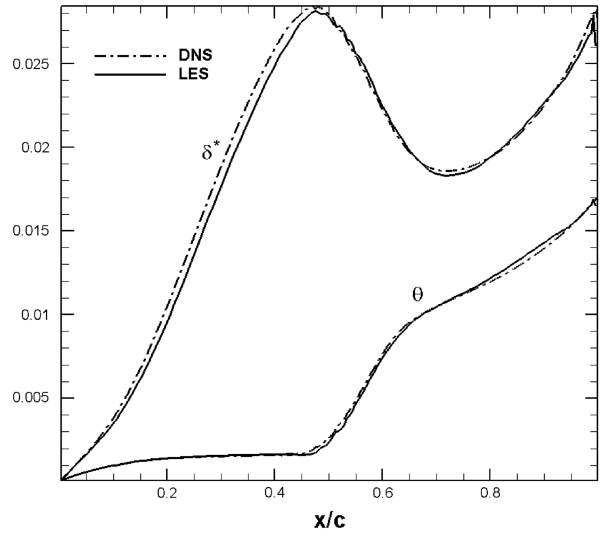

Fig. 7 Comparison of displacement and momentum thickness between DNS and LES ($\alpha = 5$ deg, without SGS).

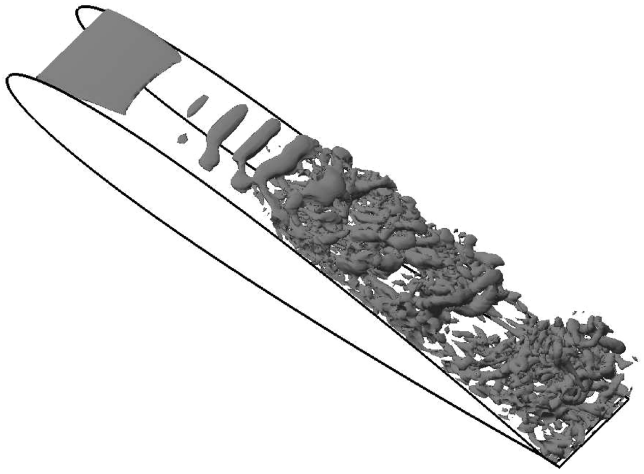

Fig. 8 Three-dimensional isosurface of second invariant of the velocity gradient at $Q = 100$ obtained by LES ($\alpha = 5$ deg, without SGS).

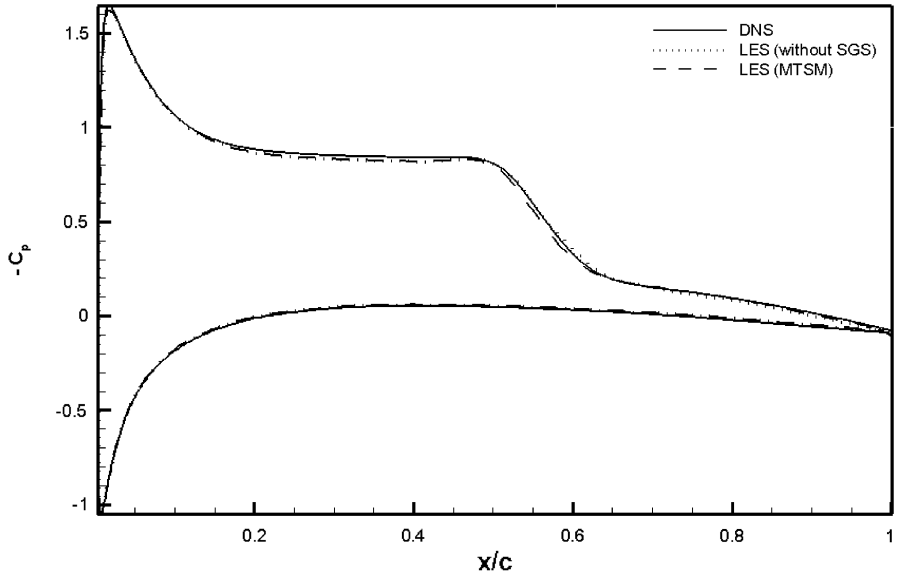

Fig. 9 Comparison of pressure coefficients between DNS, LES without SGS model, and LES using the MTS model ($\alpha = 5$ deg).

grids of $637 \times 320 \times 32$ with various angles of attack were generated. The primary grid parameters of the 3-D simulation are summarized in Table 3, where LES_narrow refers to the large-eddy simulation with a narrow computational domain $L_z = 0.2c$, and LES_wide to a large-eddy simulation with a wide computational domain $L_z = 0.5c$.

Using the MTS model, LES calculations were performed to produce aerodynamic data. The spanwise length of the airfoil model was initially set at 20% of the chord length (case LES_narrow).

The series of tests started with $\alpha = 11$ deg, where the flow is found to be fully separated and no oscillation was observed. Then the angle of attack was decreased to 10 deg, and the 3-D simulation was restarted from the 2-D results at the same incidence, leading to another fully separated flow solution. In contrast to the 11 and 10 deg cases, the simulations at angles of attack of 8.5 and 8.9 deg exhibit a flow that always attaches to the airfoil suction side without bursting of the separation bubble. Therefore, any low-frequency oscillation may occur only in the narrow range of 8.9 to 10 deg.

The time history for the lift coefficient for LES_narrow at $\alpha = 9.25$ deg demonstrates rapid airfoil stalling after nine time units (Fig. 11 LES_narrow line), where the lift coefficient drops dramatically (54.7% reduction) from its maximum value of 0.895 at $t = 4$ to 0.405 at $t = 17$. At this stage the laminar separation bubble, located near the leading edge, bursts, and the flow becomes fully separated from the surface of the airfoil. The flow reattaches for $t > 44$, and the lift increases until it reaches a second maximum value of 0.815 at $t = 62.5$. The lift then dropped again to 0.43 at $t = 72$, after which the oscillations cease and the flow remains fully stalled.

The issue of the spanwise computational domain size was discussed by Eisenbach and Friedrich [30] who found, in their study of an incompressible flow around an NACA-4415 airfoil at $Re = 1 \times 10^4$ and incidence of 18 deg, that the spanwise lengths of the largest turbulent flow structures near the trailing edge were approximately 66% of the chord length. Therefore, the spanwise length of the current computational domain was extended to 50% of the chord length and a further simulation (LES_wide) was carried out to investigate the effect of the spanwise domain width on the behavior of the flow. The main grid parameters for this simulation were presented in Table 3. It should be noted that the domain widths provided here are already large compared with previous LES. For example, Mary and Sagaut [31] conducted an LES with very small spanwise extents ($L_z/c \leq 0.005$, 0.012, and 0.03) and different resolutions, to simulate a flow past an airfoil at a Reynolds number of 2.1×10^6 and incidence of 13.3 deg. They found that there was a

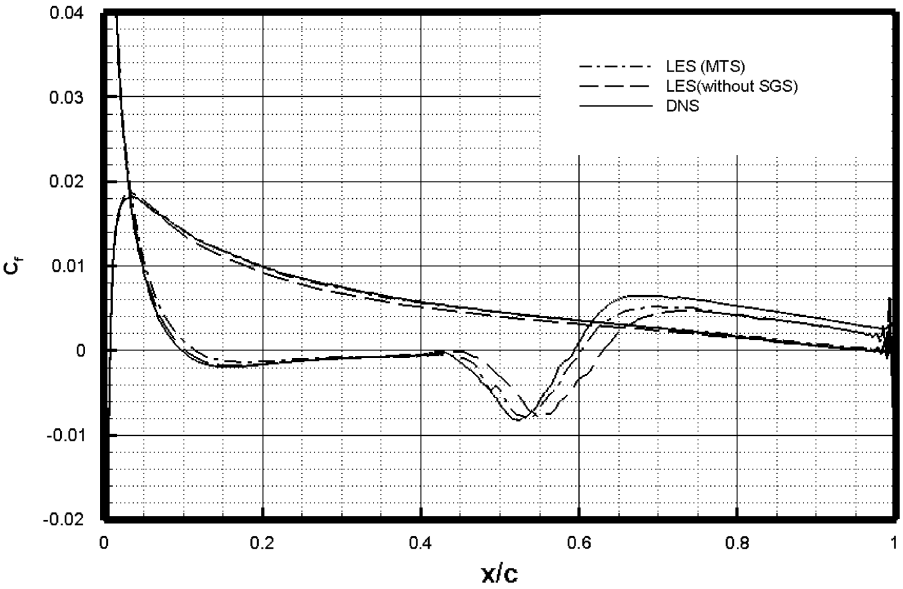

Fig. 10 Comparison of skin-friction coefficients between DNS, LES without SGS model, and LES using the MTS model ($\alpha = 5$ deg).

Table 3 Grid parameters for LES at $Re = 50,000$ and $\alpha = 9.25$ deg

Simulation	W	R	Total length	N_ξ	N_η	N_z	L_z/c	Ps	SS	NW	Total points
LES_narrow	5	7.3	14.2	637	320	32	0.2	130	170	170	6522880
LES_wide	5	7.3	14.2	637	320	80	0.5	130	170	170	16307200

great improvement in the results compared with the experiment results when the width of the computational domain and the numerical resolution were increased.

From the variation of the lift coefficient in Fig. 11, it can be seen that the flow behavior changed when the domain width was increased and the flow exhibits an irregular low-frequency oscillation. A comparison between the span- and time-averaged flow streamlines is shown in Fig. 12 (averaged for $64 \leq t \leq 128$), where the formation of a long separation bubble of about 60% chord is clearly seen for the LES_wide simulation, whereas the flow fails to reattach with LES_narrow. The differences imply that the domain width should be at least 50% of the chord length and possibly more. It is noted that the long bubble observed in the LES_wide simulation is longer than the 35% chord bubble that reported by Rinoie and Takemura [8], which is attributed to the higher Reynolds number ($Re = 130,000$) used in the experiments. It is concluded that the laminar separation bubble is very sensitive to incidence, Reynolds number, and L_z.

The effect of L_z can be studied in more detail using the two-point velocity correlation function:

$$R_{uu}(z_1) = \langle u'(z)u'(z+z_1)\rangle / \langle u'(z)u'(z)\rangle \tag{17}$$

where $\langle\,\rangle$ denotes averaging over z and time, u' is the streamwise velocity fluctuation, and z_1 denotes the correlation distance. Figures 13a and 13b show the two-point velocity correlations at seven different locations on the suction side of the airfoil, obtained by the LES_narrow and LES_wide simulations, respectively. The worst correlation value ($R_{uu} \approx -0.56$) was observed in the trailing edge of the narrower domain, compared with ($R_{uu} \approx -0.28$) in the trailing edge of the wider domain. This means that a significant improvement was achieved by extending the width of the computational domain. The present simulation requires a wider computation domain compared with Mellen et al. [32], who applied LES to simulate a flow around an Aerospatiale A-airfoil with Reynolds number $Re = 2.1 \times 10^6$ and $\alpha = 13.3$ deg. They recommended a minimum $L_z = 0.12c$ for a case at higher Reynolds number with small trailing-edge separation. The presence of a large region of separation in the present configuration compared with [32], which only had a small trailing-edge separation, is almost certainly the reason for the difference.

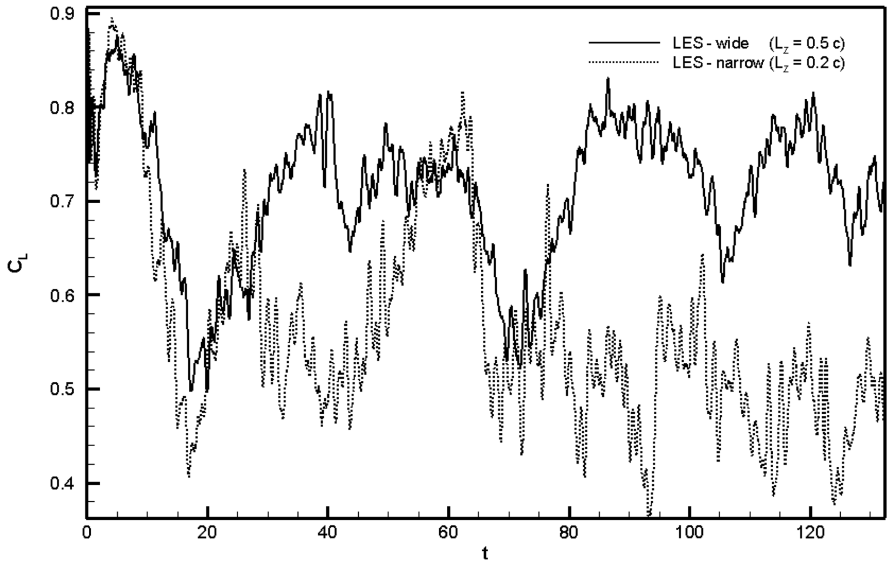

Fig. 11 Effect of increasing the spanwise length of the computational domain on the LES time dependence lift coefficient for an angle of $\alpha = 9.25$ deg.

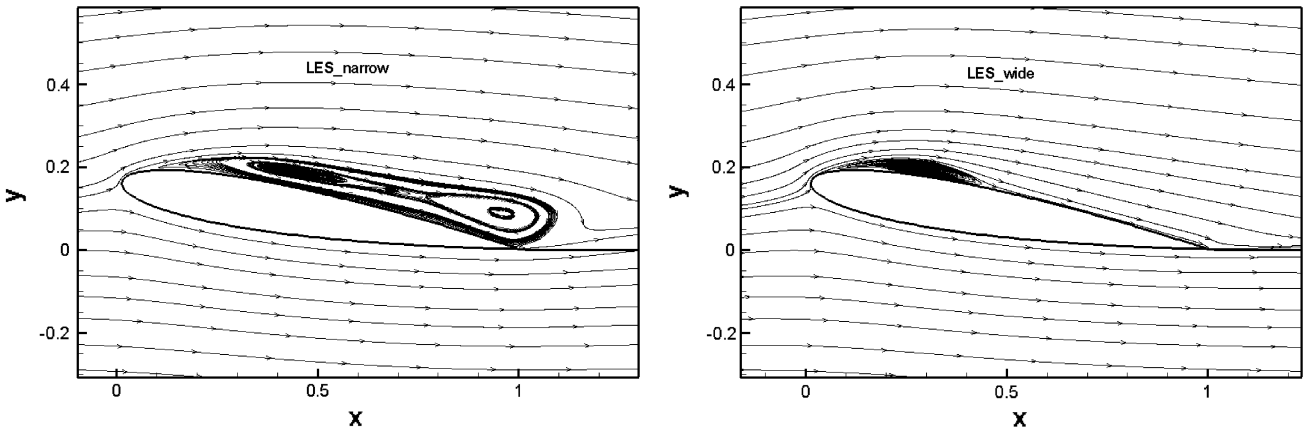

a) b)

Fig. 12 Streamlines patterns for time and span averaged velocity over long time interval ($64 \leq t \leq 128$) for $\alpha = 9.25$ deg, obtained from the a) narrow, and b) wide domain simulations.

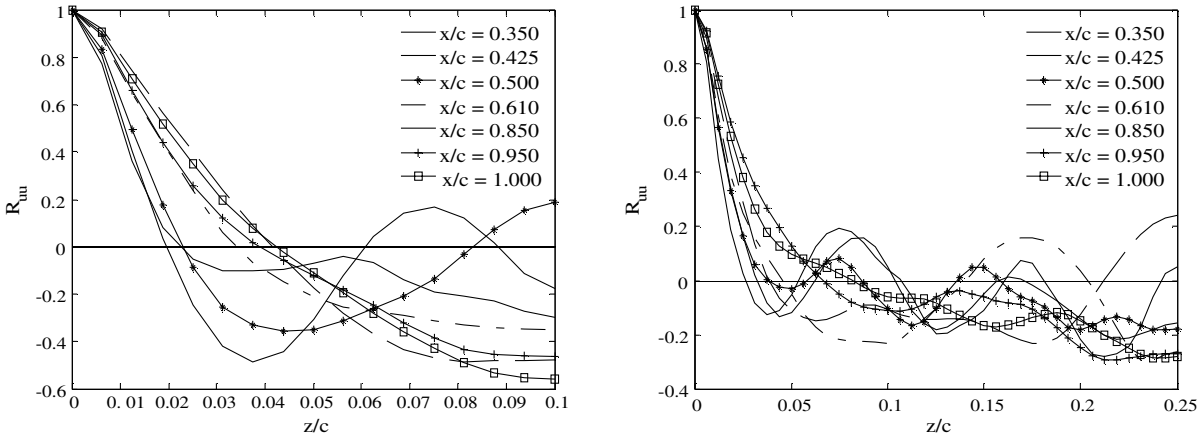

Fig. 13 Two-point velocity correlations based on the streamwise velocity obtained by a) LES_narrow, and b) LES_wide for $\alpha = 9.25$ deg.

The present results indicate that LES of airfoil flows (e.g., [33], which used $L_z = 0.2c$) need careful attention to spanwise domain width near stall.

Previous studies of low-frequency flow oscillation [8,9] showed regular oscillations, whereas the laminar separation bubble here is more irregular, with intermittent bursting to form either a long bubble or a fully separated flow. For example, the streamlines patterns for time and span averaged velocity between $t = 4.8$ and $t = 6.4$ revealed a laminar separation bubble of approximately 25% of the chord located near the leading edge (Fig. 14a). This then bursts to create a fully stalled flow at $t = 20.8$, as shown in Fig. 14b. This process was repeated between $t \approx 58.0$ and $t \approx 70.0$.

Different behavior of laminar separation bubbles was observed between $t = 74.9$ and $t = 108.8$ (Fig. 15). The formation of the laminar separation bubble of approximately 35% of the chord length was clearly seen from $t = 74.9$ to $t = 88$. After that, bursting occurred to form a long separation bubble of approximately 65% of the chord length, in conjunction with a low lift coefficient ($C_L \approx 0.615$). The length of the shortest laminar separation bubble (25% chord) is longer than the short bubble reported by Rinoie and Takemura [8] which was 10% chord. In addition, it is noticeable from Fig. 15 that the flow exhibits a trailing-edge separation at the end of the oscillation cycle. This is in agreement with the observation of Broeren and Bragg [7] for the flow around the LRN-1007 airfoil regarding the growth of the leading-edge separation bubble and trailing-edge separation until they merged. The difference here is that the trailing-edge separation does not always lead to a fully stalled flow. On the other hand, Rinoie and Takemura [8] did not mention this type of turbulent separation. Figure 16 shows a time history of the spanwise averaged separation and reattachment locations from $t = 43$ to $t = 133$, where the irregular unsteady laminar separation bubble and the fully separated flow are clearly seen.

Surface pressure distributions, averaged over selected intervals, are depicted in Fig. 17 where significant unsteadiness of the pressure can be observed. The reattachment of the flow and the formation of the laminar separation bubble occurred when the suction peak ($-C_p$) was increasing from the first interval ($74.9 \leq t \leq 76.5$) until it reached a maximum value for the interval ($86.4 \leq t \leq 88.0$). Subsequently, the bubble burst caused a drop in the suction peak but never reached the same level of the first interval, where the flow was fully stalled.

The Strouhal number based on the cycle $74.9 \leq t \leq 108.8$ is 0.00466 ($Re = 50,000$ and $\alpha = 9.25$ deg), compared with 0.008 as reported by Rinoie and Takemura [8] (at $\alpha = 11.5$ deg, $Re = 130,000$), who used a higher incidence and Reynolds number.

VI. Unsteady Viscous-Inviscid Interaction Results

The principle of the present unsteady viscous-inviscid interaction method is to couple the potential flow solution, which can be obtained by a panel method, with the viscous solution of the integral boundary-layer equations, which contains models of laminar flow, turbulent flow, and transition. Viscous-inviscid interaction is very cheap compared with numerical methods that solve the Navier–Stokes equations. Usually this numerical technique was implemented only for steady flow [4]. Sandham [9] made a modification to the viscous-inviscid method to solve an unsteady formulation of the momentum integral equation. This enables study of the unsteadiness of the laminar-turbulent transitional flows and thus some of the aerodynamic

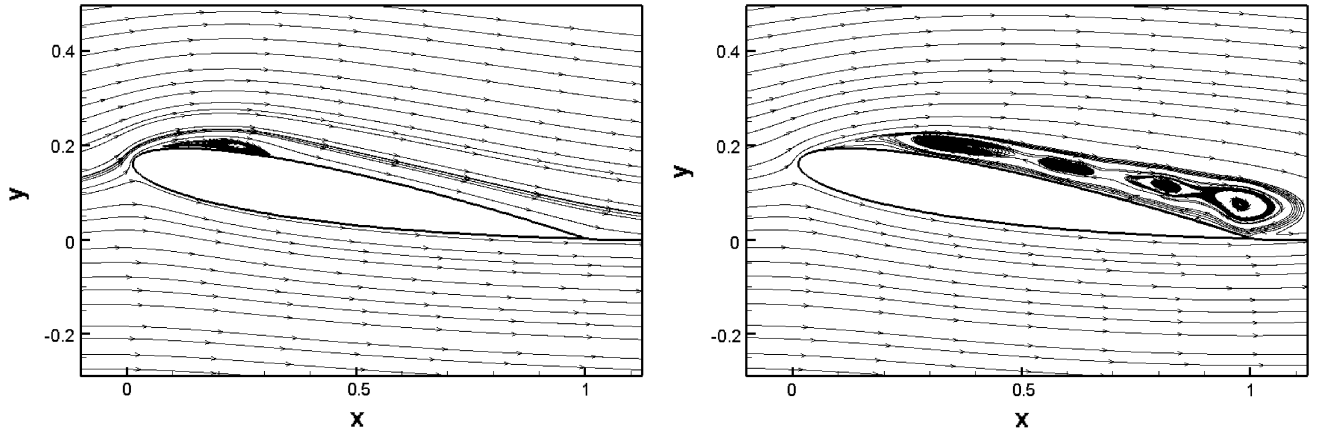

Fig. 14 Streamline patterns for time and span averaged flow around a NACA 0012 at $\alpha = 9.25$ deg, obtained from LES_wide over the intervals: a) $4.8 \leq t \leq 6.4$, and b) $19.2 \leq t \leq 20.8$.

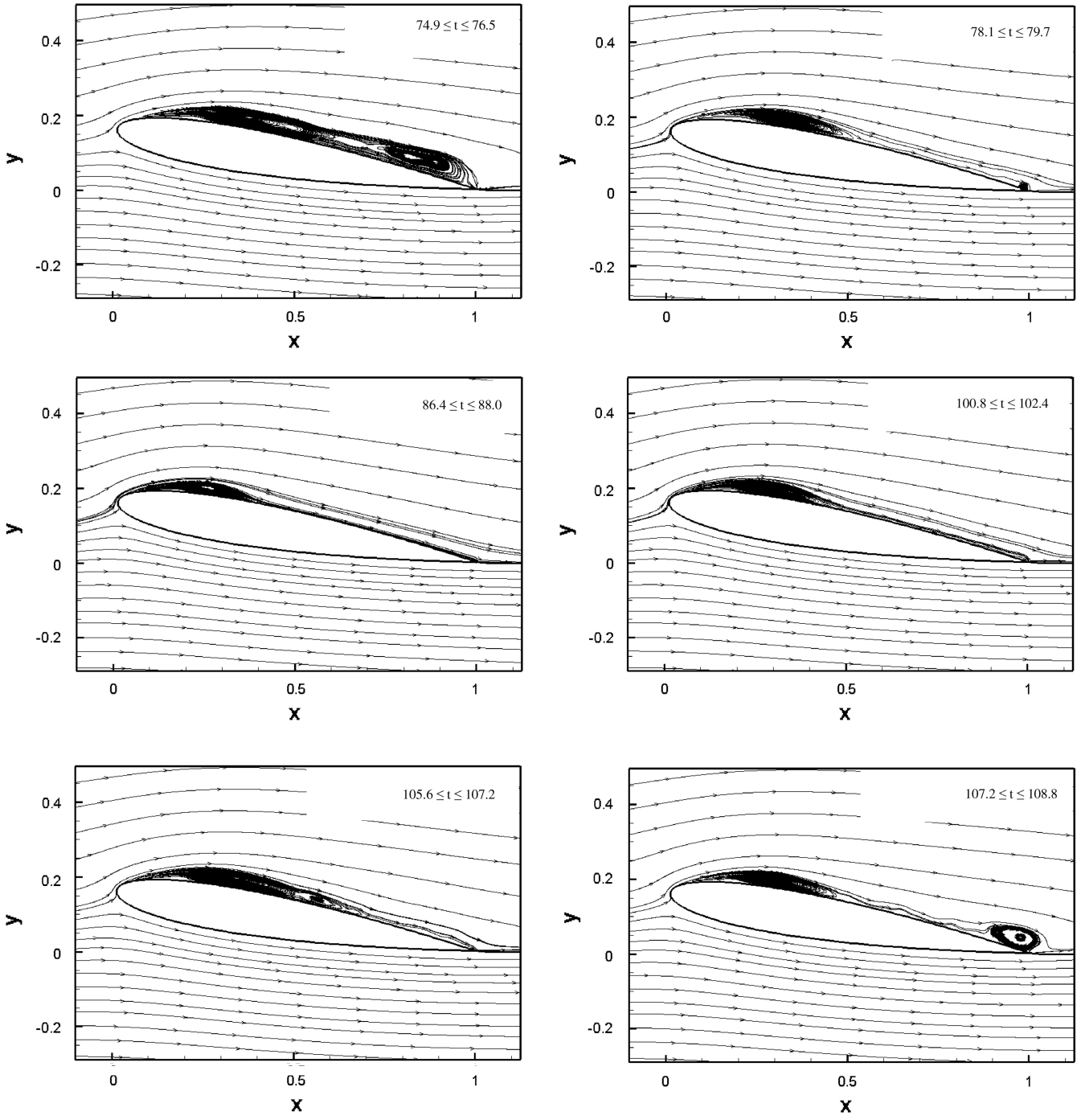

Fig. 15 Streamline patterns for span and short-time-averaged flow around a NACA 0012 at $\alpha = 9.25$ deg, obtained from LES_wide over the selected intervals from $t = 74.9$ to $t = 108.8$, showing the formation of separation zones.

characteristics of the low-frequency behavior of the laminar separation bubble near stall.

A. Governing Equations of the Viscous-Inviscid Interaction Method

The main governing equation is the unsteady form of the momentum integral equation:

$$\frac{\partial U\delta^*}{\partial t} + \frac{\partial U^2\theta}{\partial s} + U\delta^*\frac{\partial U}{\partial s} = \frac{\tau_w}{\rho} \tag{18}$$

where s is the airfoil surface coordinate. The interaction condition for Eq. (18) is the surface transpiration velocity:

$$v_s = d(U\delta^*)/d(s) \tag{19}$$

which can be solved and imposed as a boundary condition for the potential flow. The viscous flow calculations are applied by modelling the shape factor $H = \delta^*/\theta$, the entrainment E [34], and the amplification factor n [4] according to the following transport equations:

$$\frac{\partial H}{\partial t} + U_H\frac{\partial H}{\partial s} = B_H \tag{20}$$

$$\frac{\partial E}{\partial t} + U_E\frac{\partial E}{\partial s} = B_E \tag{21}$$

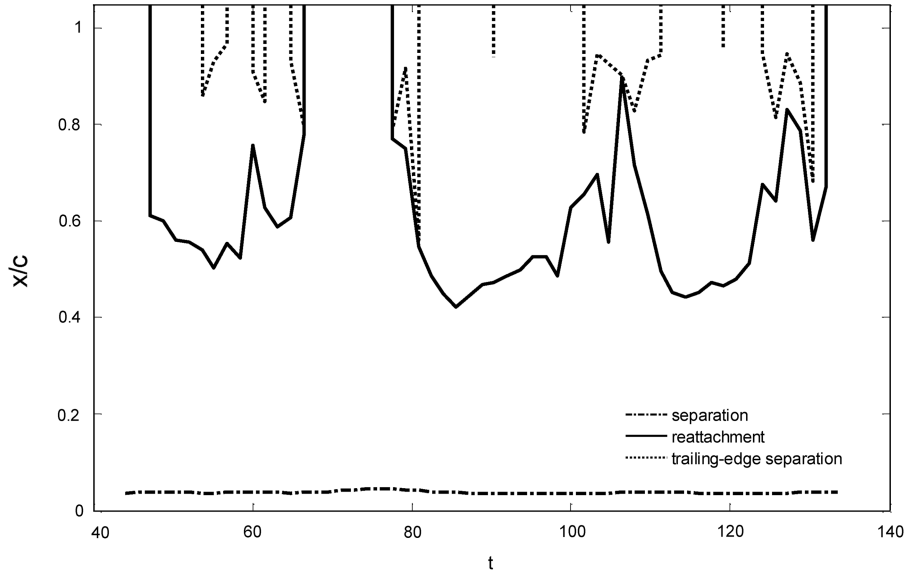

Fig. 16 Separation and reattachment locations for the laminar separation bubble during the low-frequency flow oscillation at $\alpha = 9.25$ deg.

$$\frac{\partial n}{\partial t} + U_n \frac{\partial n}{\partial s} = B_n \tag{22}$$

where U_H, U_E, and U_n are convective velocities and B_H, B_E, and B_n include laminar and turbulent boundary-layer models and a laminar-turbulent transition model based on the growth of the amplification factor n via boundary-layer instability (see [9] for more modelling details). When the amplification factor goes beyond a critical value n_{crit} the flow becomes fully turbulent. The present results were obtained with $n_{\text{crit}} = 9$ and 120 panels. The calculations were run for 40 time units to ensure that the solution passed the transient flow region. The viscous-inviscid interaction lift coefficients revealed low-frequency oscillations from which the peak-to-peak amplitude and Strouhal number were extracted.

B. Viscous-Inviscid Interaction Results

To determine the relationships between incidence, Reynolds number, and Strouhal number that govern the behavior of the laminar separation bubble near stall, the unsteady viscous-inviscid modelling method was employed over a wide range of Reynolds numbers. At each Re, the incidence was increased through the stall regime. Low-frequency modes were only detected between $Re = 50,000$ and $Re = 420,000$; beyond this range, the airfoil stalled suddenly. Figure 18 shows the Strouhal number as a function of incidence for all the cases in which the low-frequency flow oscillation phenomenon was observed. For comparison, the results of LES and experiments [8] are included. It can be seen from this figure that the magnitude of the Strouhal number obtained by the viscous-inviscid interaction method increases as the Reynolds number, and hence incidence of stall, increased. It is also clear that there is a variation of the Strouhal number at each Reynolds number, but the general trend shows an increase until it reaches a maximum Strouhal number ($St = 0.015$) at $Re = 300,000$ and $\alpha = 13.4$ deg. A significant drop is then observed at $Re = 420,000$, and any further increase in Re leads to the disappearance of the low-frequency flow oscillation phenomenon. Figure 18 also shows that Strouhal number of LES and experiment follow similar trends with the viscous-inviscid interaction results, although their values are smaller.

Another relationship that can be deduced from the viscous-inviscid method is between the incidence and the peak-to-peak amplitude of the lift coefficient in the low-frequency flow oscillation, as illustrated in Fig. 19. The peak-to-peak amplitude increases in a similar fashion to the Strouhal number in Fig. 18 as the incidence is

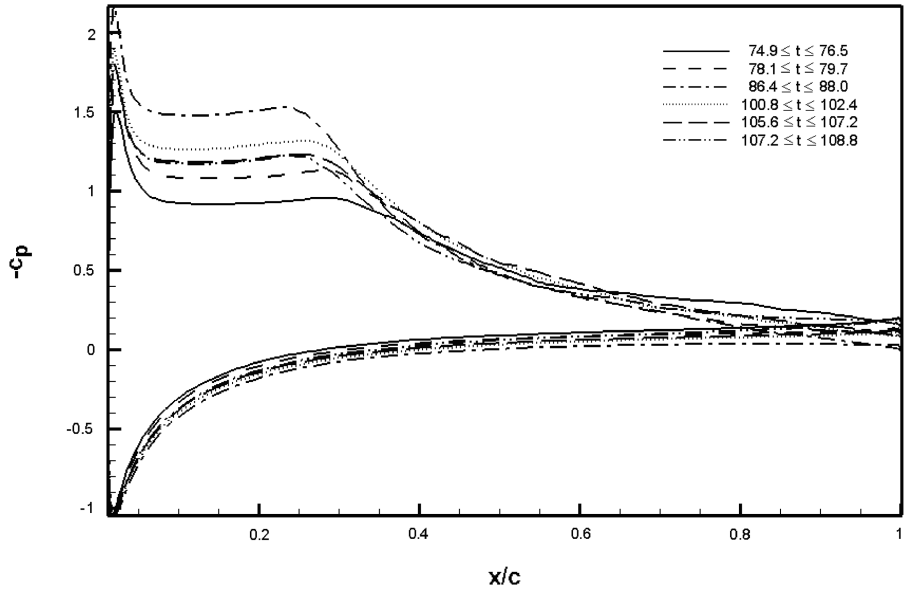

Fig. 17 Pressure coefficients for the captured cycle of low-frequency flow oscillation at $\alpha = 9.25$ deg obtained from the LES_wide simulation.

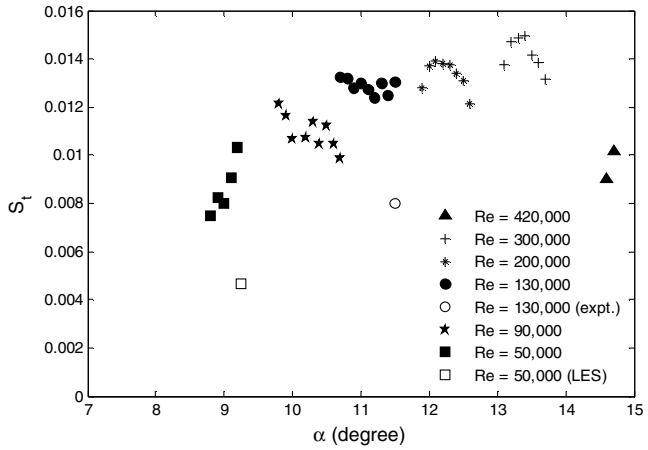

Fig. 18 The relationship between the incidence and the Strouhal number of the low-frequency flow oscillation.

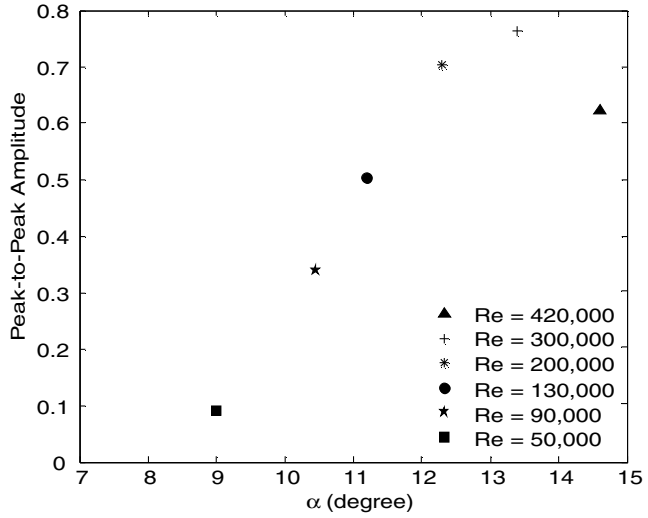

Fig. 19 The relationship between the incidence and the peak-to-peak amplitude of low-frequency flow oscillation.

increased. The peak-to-peak amplitude is also increased as the Reynolds number is increased, as seen in Fig. 20, which also shows that the LES amplitude is larger than that obtained by the viscous-inviscid interaction method. Figure 21 shows that the incidence corresponding to the maximum Strouhal number increases significantly with the Reynolds number, which is in agreement with the

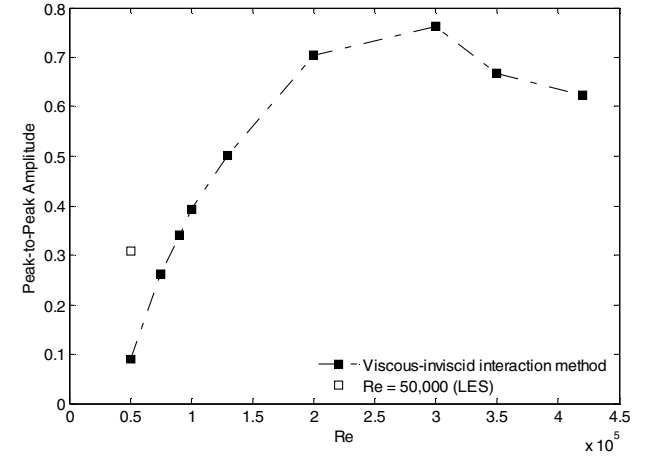

Fig. 20 The relationship between the Reynolds number and the peak-to-peak amplitude of low-frequency flow oscillation, and a comparison between the LES and the viscous-inviscid method results.

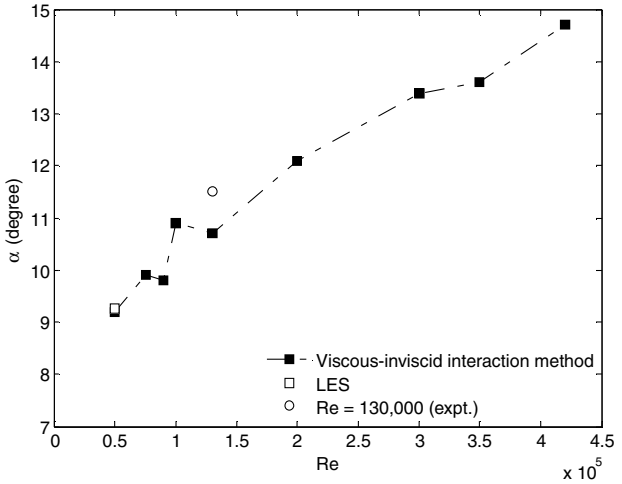

Fig. 21 The relationship between the Reynolds number and the incidence of low-frequency flow oscillation, and a comparison between the experiment, LES and the viscous-inviscid method results.

observation of Bragg et al. [6]. Overall the trends from the viscous-inviscid interaction method are consistent with the limited data currently available from LES and experiment. Further LES over a wider range of parameters should allow the viscous-inviscid interaction method to be improved. Peak amplitudes of 0.75 are comparable to Zaman et al. [5], whereas the Strouhal number for the NACA 0012 seems to be lower than for the E374 airfoil [6,7,35].

VII. Conclusions

Large-eddy simulation has been performed to study the behavior of laminar separation bubbles near stall. For a validation case the LES results compare favorably with DNS. The LES captures the most important physical phenomena, including the separation of the boundary layer from airfoil surface, vortex shedding, breakdown to turbulence, and low-frequency flow oscillation. There is a small improvement when a mixed-time-scale subgrid model is included, compared with the case of filtering alone. Transient low-frequency flow behavior has been found at $Re = 50,000$ and $\alpha = 9.25$ deg but eventually the flow became fully stalled in the narrower computational domain simulation. Increasing the computational domain width to 50% of the chord length was found to be necessary to obtain a reasonable decay of two-point correlations. The results of LES with the wider domain have revealed an intermittent bursting of the laminar separation bubble near stall, to form either a long bubble or fully separated flow. This demonstrates that LES can provide useful results compared with the experiment, provided computational requirements such as the resolution and the spanwise extent are met properly. Low-frequency behavior was observed between $Re = 50,000$ and $Re = 420,000$ using an unsteady viscous-inviscid interaction method. The peak-to-peak amplitude and the Strouhal number for the low-frequency flow oscillation were found to be dependent on Reynolds number and incidence. The demonstrated capability of LES for airfoil simulations of low-Reynolds number should enable improvements to be made to cheaper computational approaches such as viscous-inviscid interaction and RANS.

References

[1] McCullough, G. B., and Gault, D. E., "Examples of Three Representative Types of Airfoil-Section Stall at Low Speed," NACA TN 2502, 1951.

[2] Gaster, M., "The Structure and Behavior of Laminar Separation Bubbles," Aeronautucal Research Council R&M 3595, 1967.

[3] Horton, H. P., "A Semi-Empirical Theory for the Growth and Bursting of Laminar Separation Bubbles," Aeronautical Research Coucil CP 1073, 1967.

[4] Drela, M., and Giles, M. B., "Viscous-Inviscid Analysis of Transonic and Low Reynolds Number Airfoils," *AIAA Journal*, Vol. 25, No. 10, 1987, pp. 1347–1355.

doi:10.2514/3.9789
[5] Zaman, K. B. M. Q., Mckinzie, D. J., and Rumsey, C. L., "A Natural Low-Frequency Oscillation of The Flow Over an Airfoil Near Stalling Conditions," *Journal of Fluid Mechanics*, Vol. 202, 1989, pp. 403–442. doi:10.1017/S0022112089001230
[6] Bragg, M. B., Heinrich, D. C., Balow, F. A., and Zaman, K. B. M. Q., "Flow Oscillation over an Airfoil Near Stall," *AIAA Journal*, Vol. 34, No. 1, 1996, pp. 199–201. doi:10.2514/3.13045
[7] Broeren, A. P., and Bragg, M. B., "Flowfield Measurements Over an Airfoil During Natural Low-Frequency Oscillations Near Stall," *AIAA Journal*, Vol. 37, No. 1, 1999, pp. 130–132. doi:10.2514/2.678
[8] Rinoie, K., and Takemura, N., "Oscillating Behaviour of Laminar Separation Bubble Formed on an Aerofoil Near Stall," *The Aeronautical Journal*, Vol. 108, 2004, pp. 153–163.
[9] Sandham, N. D., "Transitional Separation Bubbles and Unsteady Aspects of Aerofoil Stall," *The Aeronautical Journal*, Vol. 112, No. 1133, 2008, pp. 395–404.
[10] Pauley, L. L., Moin, P., and Reynolds, W. C., "The Structure of Two-Dimensional Separation," *Journal of Fluid Mechanics*, Vol. 220, 1990, pp. 397–411. doi:10.1017/S0022112090003317
[11] Alam, M., and Sandham, N. D., "Direct Numerical Simulation of "Short" Laminar Separation Bubbles With Turbulent Reattachment," *Journal of Fluid Mechanics*, Vol. 403, 2000, pp. 223–250. doi:10.1017/S0022112099007119
[12] Spalart, P. R., and Strelets, M. K., "Mechanisms of Transition and Heat Transfer in a Separation Bubble," *Journal of Fluid Mechanics*, Vol. 403, 2000, pp. 329–349. doi:10.1017/S0022112099007077
[13] Yang, Z., and Voke, P. R., "Large-Eddy Simulation of Boundary-Layer Separation and Transition at a Change of Surface Curvature," *Journal of Fluid Mechanics*, Vol. 439, 2001, pp. 305–333. doi:10.1017/s0022112001004633
[14] Hoarau, Y., Faghani, D., Braza, M., Perrin, R., Ann-Archard, D., and Ruiz, D., "Direct Numerical Simulation of the Three-Dimensional Transition to Turbulence in the Incompressible Flow Around a Wing," *Flow, Turbulence and Combustion*, Vol. 71, Nos. 1–4, 2003, pp. 119–132. doi:10.1023/B:APPL.0000014931.01400.7e.
[15] Yuan, W., Xu, H., Khalid, M., and Radespiel, R., "A Parametric Study of LES on Laminar-Turbulent Transitional Flows Past an Airfoil," *International Journal of Computational Fluid Dynamics*, Vol. 20, No. 1, 2006, pp. 45, 54. doi:10.1080/10618560600578492
[16] Jones, L. E., Sandberg, R. D., and Sandham, N. D., "Direct Numerical Simulation of Forced and Unforced Separation Bubbles on an Airfoil at Incidence," *Journal of Fluid Mechanics*, Vol. 602, 2008, pp. 175–207. 10.1017/20022112008000864
[17] Zhang, W., Hain, R., and Kähler, C. J., "Scanning PIV Investigation of the Laminar Separation Bubble on a SD7003 Airfoil," *Experiments in Fluids*, Vol. 45, No. 4, 2008, pp. 725–743. doi:10.1007/s00348-008-0563-8
[18] Windte, J., Scholz, U., and Radespiel, R., "Validation of the RANS-Simulation of Laminar Separation Bubbles on Airfoil," *Aerospace Science and Technology*, Vol. 10, No. 6, 2006, pp. 484–494. doi:10.1016/j.ast.2006.03.008
[19] Inagaki, M., Kondoh, T., and Nagano, Y., "A Mixed-Time-Scale SGS Model with Fixed Model-Parameters for Practical LES," *Journal of Fluids Engineering*, Vol. 127, No. 1, 2005, pp. 1–13. doi:10.1115/1.1852479.
[20] Krishnan, L., Sandham, N. D., and Steelant, J., "Shock-Wave/Boundary-Layer Interactions in a Model Scramjet Intake," *AIAA Journal*, 10.2514/1.41107 to be published.
[21] Sandham, N. D., Li, Q., and Yee, H. C., "Entropy Splitting for High-Order Numerical Simulation of Compressible Turbulence," *Journal of Computational Physics*, Vol. 178, No. 2, 2002, pp. 307–322. doi:10.1006/jcph.2002.7022
[22] Carpenter, M. H., Nordstrom, J., and Gottlieb, D., "A Stable and Conservative Interface Treatment of Arbitrary Spatial Accuracy," *Journal of Computational Physics*, Vol. 148, No. 2, 1999, pp. 341–365. doi:10.1006/jcph.1998.6114
[23] Lele, S. K., "Compact Finite-Difference Scheme with Spectral-Like Resolution," *Journal of Computational Physics*, Vol. 103, 1992, pp. 16–42. doi:10.1016/0021-9991(92)90324-R
[24] Visbal, M. R., and Rizzetta, D. P., "Large Eddy Simulation on Curvilinear Grids Using Compact Differencing and Filtering Schemes," *Journal of Fluids Engineering*, Vol. 124, No. 4, 2002, pp. 836, 847. doi:10.1115/1.1517564
[25] Bogey, C., and Bailly, C., "A Family of Low Dispersive and Low Dissipative Explicit Schemes for Flow and Noise Computations," *Journal of Computational Physics*, Vol. 194, No. 1, 2004, pp. 194–214. doi:10.1016/j.jcp.2003.09.003
[26] Jones, L., E., "Numerical Studies of the Flow Around an Airfoil at Low Reynolds Number," Ph.D. Thesis, School of Engineering Sciences, Univ. of Southampton, Southampton, England, UK, 2007.
[27] Sandhu, H. S., and Sandham, N. D., "Boundary Conditions for Spatially Growing Compressible Shear Layer," Faculty of Engineering, University of London, Rep. QMW-EP-1100, London, England, U.K., 1994.
[28] Sandberg, R. D., and Sandham, N. D., "Nonreflecting Zonal Characteristic Boundary Condition for Direct Numerical Simulation of Aerodynamic Sound ," *AIAA Journal*, Vol. 44, No. 2, 2006, pp. 402–405. doi:10.2514/1.19169
[29] Ripley, M. D., and Pauley, L. L., "The Unsteady Structure of Two-Dimensional Steady Laminar Separation," *Physics of Fluids*, Vol. 5, No. 12, 1993, pp. 3099–3106. doi:10.1063/1.858719.
[30] Eisenbach, S., and Friedrich, R., "Large-Eddy Simulation of Flow Separation on an Airfoil at a High Angle of Attack and $Re = 105$ Using Cartesian Grids," *Theoretical and Computational Fluid Dynamics*, Vol. 22, No. 3–4, 2008, pp. 213–225. doi:10.1007/s00162-007-0072-z
[31] Mary, I., and Sagaut, P., "Large Eddy Simulation of Flow Around an Airfoil near Stall," *AIAA Journal*, Vol. 40, No. 6, 2002, pp. 1139–1145. doi:10.2514/2.1763
[32] Mellen, C. P., Fröhlich, J., and Rodi, W., "Lessons from LESFOIL Project on Large-Eddy Simulation of Flow Around an Airfoil," *AIAA Journal*, Vol. 41, No. 4, 2003, pp. 573–581. doi:10.2514/2.2005
[33] You, D. Y., Ham, F., and Moin, P., "Discrete Conservation Principles in Large-Eddy Simulation with Application to Separation Control Over and Airfoil," *Physics of Fluids*, Vol. 20, No. 10, 2008, article 101515. doi:10.1063/1.3006077
[34] Green, J. E., Weeks, D. J., and Brooman, J. W. F., "Prediction of Turbulent Boundary Layers and Wakes in Compressible Flow by a Lag-Entrainment Method," Aeronautical Research Council R&M 3791, 1977.
[35] Broeren, A. P., and Bragg, M. B., "Spanwise Variation in the Unsteady Stalling Flowfields of Two-Dimensional Airfoil Models," *AIAA Journal*, Vol. 39, No. 9, 2001, pp. 1641–1651. doi:10.2514/2.1501

D. Gaitonde
Associate Editor